An interfacial self-assembling bioink for the manufacturing of capillary-like structures with tuneable and anisotropic permeability

IOP Publishing Biofabrication 13 (2021) 035027 https://doi.org/10.1088/1758-5090/abe4c3

Biofabrication

OPEN ACCESS

RECEIVED
30 September 2020

REVISED
25 January 2021

ACCEPTED FOR PUBLICATION
9 February 2021

PUBLISHED
8 April 2021

PAPER

An interfacial self-assembling bioink for the manufacturing of capillary-like structures with tuneable and anisotropic permeability

Yuanhao Wu[1,2,3,4], Gabriele Maria Fortunato[5], Babatunde O Okesola[3,4], Francesco Luigi Pellerej Di Brocchetti[5], Ratima Suntornnond[6], John Connelly[6], Carmelo De Maria[5], Jose Carlos Rodriguez-Cabello[7], Giovanni Vozzi[5], Wen Wang[3,4] and Alvaro Mata[1,2,3,4,8]

[1] School of Pharmacy, University of Nottingham, Nottingham NG7 2RD, United Kingdom
[2] Biodiscovery Institute, University of Nottingham, Nottingham NG7 2RD, United Kingdom
[3] Institute of Bioengineering, Queen Mary University of London, London E1 4NS, United Kingdom
[4] School of Engineering and Materials Science, Queen Mary University of London, London E1 4NS, United Kingdom
[5] Research Center 'E. Piaggio' and Dipartimento di Ingegneria dell'Informazione, University of Pisa, Largo Lucio Lazzarino, Pisa 1-56122, Italy
[6] CREATE LAB, Blizard Institute, Barts and the London School of Medicine and Dentistry, Queen Mary University of London, London E1 2AT, United Kingdom
[7] BIOFORGE Group, University of Valladolid, CIBER-BBN, Valladolid 47011, Spain
[8] Department of Chemical and Environmental Engineering, University of Nottingham, Nottingham NG7 2RD, United Kingdom

E-mail: a.mata@nottingham.ac.uk

Keywords: self-assembling bioink, hierarchical control, 3D printing, tuneable permeability, anisotropic structure

Supplementary material for this article is available online

Abstract

Self-assembling bioinks offer the possibility to biofabricate with molecular precision, hierarchical control, and biofunctionality. For this to become a reality with widespread impact, it is essential to engineer these ink systems ensuring reproducibility and providing suitable standardization. We have reported a self-assembling bioink based on disorder-to-order transitions of an elastin-like recombinamer (ELR) to co-assemble with graphene oxide (GO). Here, we establish reproducible processes, optimize printing parameters for its use as a bioink, describe new advantages that the self-assembling bioink can provide, and demonstrate how to fabricate novel structures with physiological relevance. We fabricate capillary-like structures with resolutions down to $\sim$10 μm in diameter and $\sim$2 μm thick tube walls and use both experimental and finite element analysis to characterize the printing conditions, underlying interfacial diffusion-reaction mechanism of assembly, printing fidelity, and material porosity and permeability. We demonstrate the capacity to modulate the pore size and tune the permeability of the resulting structures with and without human umbilical vascular endothelial cells. Finally, the potential of the ELR-GO bioink to enable supramolecular fabrication of biomimetic structures was demonstrated by printing tubes exhibiting walls with progressively different structure and permeability.

1. Introduction

Bioinks are increasingly playing a leading role in the quest for recreating the structures and functions of biological systems [1]. These materials are being engineered to push biofabrication boundaries such as the development of thick vascularized structures [2], precise complex geometries [3], or multicellular environments [4]. However, in spite of these advances, important challenges remain such as the capacity to replicate the molecular diversity, structural hierarchy from the nano- to the macroscale, physiological biomechanical properties, and ultimate functionality of the extracellular matrix (ECM) [5] and corresponding tissues [6, 7]. Consequently, it is essential to develop innovative bioinks based on molecular and nanoscale building blocks capable of organizing hierarchically [8] and enabling communication between cellular and extracellular components [9].

Nature has evolved to grow and regenerate tissues and organs by organizing, from the bottom-up, multiple types of molecular components such as proteins, lipids, and carbohydrates [10]. Inspired by this, multicomponent self-assembly is being explored to grow materials with multiple types of molecular building-blocks exhibiting enhanced structural complexity and functionality [11]. These materials offer a unique opportunity to recreate chemical [12, 13] and mechanical features [14, 15] of the ECM and selectively communicate with cells [16]. The capacity to develop bioinks exhibiting such properties is an exciting possibility to immediately present cells [17] with complex, yet rationally designed, ECM-like milieus [18] and signals at cellular and multicellular levels [19]. Pioneering studies based on for example self-assembling peptides [17, 20, 21] or nanoparticle/polysaccharide co-assemblies [22] are demonstrating this possibility. However, the widespread use of self-assembly in additive manufacturing has been limited in large part because of inadequate standardization ensuring sufficient structural integrity, fast enough speed of setting, and scalable manufacturing [23].

Liquid-in-liquid printing, the inoculation of one low viscosity liquid phase into another [24], offers an opportunity to design bioink materials that integrate the benefits of multicomponent self-assembly with additive manufacturing in a rationally designed manner. For example, taking advantage of the interface between oil and water, nanoclay-polymer surfactants have been self-assembled into semi-permeable membranes and perfusable capillaries [24]. Also, printing a dextran water solution into a polyethylene oxide water solution enabled rapid fabrication of biocompatible tissue-like 3D architectures such as capillary networks and cardiac structures [25]. Furthermore, while traditional extrusion-based 3D printing is defined by the printing nozzle dimension, bioinks for liquid-in-liquid printing can be used to immediately set and generate structures upon liquid mixing [26], from the bottom-up, facilitating fabrication of high resolution structures. In addition, liquid-in-liquid bioinks can also be used to trigger emerging phenomena such as compartmentalization [27] and diffusion-reaction processes [28], which are used by biological systems such as cells and organelles to regulate molecular transport and assembly into functional higher-order structures. Taking advantages of these opportunities, we have recently reported on a multicomponent self-assembly mechanism harnessing disorder-to-order transitions of an elastin-like recombinamer (ELR) to non-covalently co-assemble with graphene oxide (GO) [29]. We have demonstrated the possibility to use this system in liquid-in-liquid bioprinting to enable fabrication of perfusable fluidic devices. However, it is essential to optimize printing parameters and establish reproducible processes that can demonstrate its use as a functional bioink and its advantages to fabricate physiologically-relevant functional structures.

In this study, we perform thorough top-down/bottom-up standardization of our ELR (ELK1)-GO co-assembling system to serve as a liquid-in-liquid bioink and expand on its capabilities for the fabrication (figure 1(a)) of functional capillaries down to ~10 μm in luminal diameter (figures 1(c) and (e)) and ~2 μm in wall thickness (figure 1(d)). Through experimental and cross-platform finite element analysis (COMSOL MultiPhysics® v5.5, COMSOL Group, Sweden), we demonstrate how these perfusable structures exhibit a spectrum of structural and biofunctional properties that are not possible for most bioinks including sub 10 μm size features, the capacity to pulsate, tuneable permeability with and without cells, and permeability gradients within a single structure.

2. Methods

2.1. Chemicals

Rhodamine B (⩾95%, HPLC grade) and paraformaldehyde (95%) were obtained from Sigma-Aldrich (St. Louis, Germany). GO (product number 777676) was obtained from Sigma-Aldrich. Alexa Fluor™ 488 NHS Ester (product number A20000) was obtained from Thermo Fisher Scientific (Waltham, USA). FITC-dextran 40 kDa (product number FD40), 20 kDa (product number FD20s), and fluorescein sodium salt (product number 518-47-8) were obtained from Sigma-Aldrich.

2.2. Synthesis and characterization of ELRs

ELR [ELK1: MESLLP-(VPGIG VPGIG VPGKG VPGIG VPGIG)$_{24}$] molecule was provided by TP Nanobiotechnology (Valladolid, Spain), synthesised and purified by *Escherichia coli* recombinant expression system. The sequence and molecular weights of the polymers were verified using amino acid analysis. SDS-PAGE and MALDI-TOF SIMS were used to carry out the ELK1 characterisation.

2.3. Sample preparation (ELK1-GO system)

Aqueous suspension of GO (0.1 wt%, 100 μl) was added to a well of 96-well TCP and aqueous solution of the ELK1 (2 wt%, 18 μl) was slowly injected into the suspension of GO. The tip of the pipette was allowed to contact the bottom of the well before releasing the ELK1 solution vertically at a constant speed. All samples were prepared in MilliQ water.

2.4. Diffusion-reaction of ELK1-GO tube wall formation

The diffusion-reaction of ELK1-GO tube wall formation is critical and determine the increase of tube wall thickness over time. An imaging system was used to observe tube formation and its behaviour

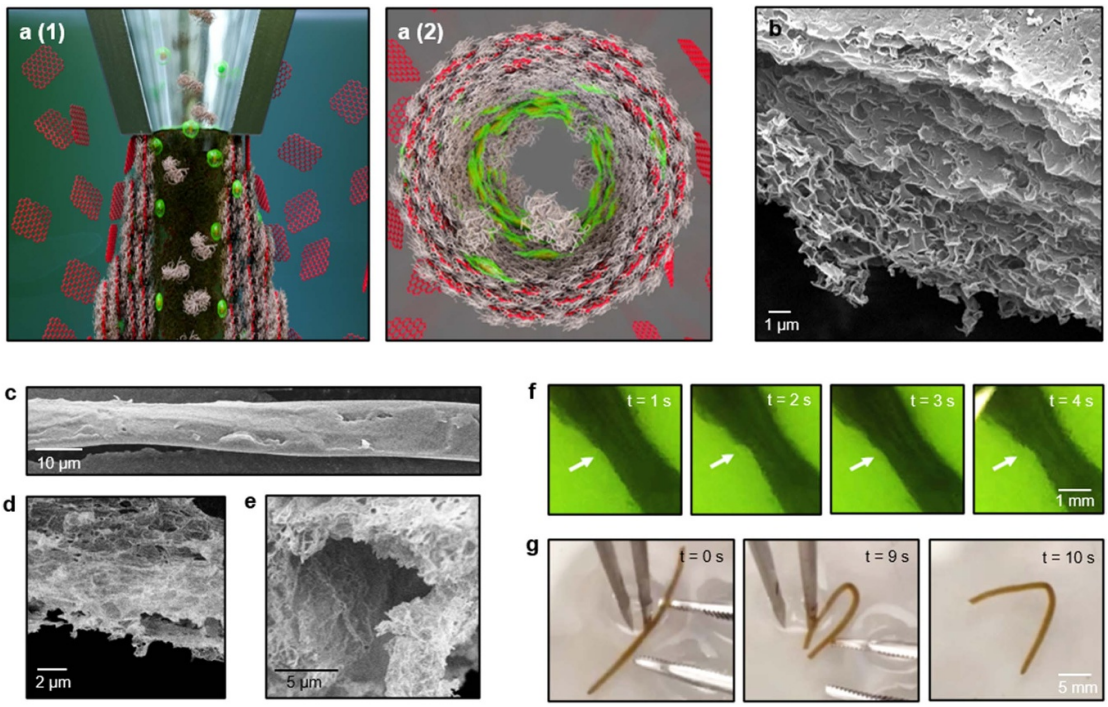

Figure1. Rationale, assembly, and structure of the ELK1-GO bioink. (a) (1) The bioink assembles upon liquid-in-liquid printing of an ELK1 (brown) solution comprising cells (green) into a solution of GO flakes (red), spontaneously triggering a diffusion-reaction process at the solution interface and leading to the formation of a multi-layered membrane. (2) The process enables trapping of cells within the membrane and immediate localization within the lumen of the resulting tubular structures. (b) Scanning electron microscope (SEM) image of the cross-section of an ELK1-GO tubular structure depicting the resulting multi-layered architecture. (c)–(e) SEM images of an ELK1-GO capillary with an internal diameter of ∼10 μm and a tube wall thickness of ∼2 μm. (f) Time-lapse imaging of an ∼1 mm diameter tube being perfused with a pulsatile (the pulse frequency was 1 Hz) flow at 12 ml min^{-1} depicting the change in tube diameter (white arrow) as a result of the material's resilient properties. (g) Time-lapse imaging of a 1 mm diameter tubular structure bent 180° and released.

over time. The system consisted of a Nikon camera with a 1:1 macro lens, a mirror to reflect the image on the lens of the camera and a light source powered at 30 V (figure S1 (available online at stacks.iop.org/BF/13/035027/mmedia)). A time lapse was used to observe the membrane self-assembly.

2.5. Confocal microscopy

The interaction and localization of ELK1 and GO was probed using laser scanning confocal and multiphoton microscopy (TCS SP2, Leica Microsystems, Germany). ELK1 (2 wt%) was dissolved in an aqueous solution of Alexa Fluor™ 488 NHS Ester (10^{-6} wt%) and GO were diluted to 0.1 wt% with an aqueous solution of Rhodamine B (10^{-6} wt%). All solutions were incubated for 20 min at 30 °C and protected from light. Images were acquired at laser wavelengths of 488 nm and 543 nm which correspond to the excitation wavelength of Alexa Fluor and Rhodamine B, respectively. Images were further processed using ImageJ.

2.6. Scanning electron microscopy (SEM)

The microstructures of ELK1-GO membranes were examined by SEM. ELK1-GO membranes were dehydrated directly using increasing concentrations of ethanol (20%, 50%, 70%, 90%, 96%, and 100%). All samples were subjected to critical point drying (K850, Quorum Technologies, UK) prior imaging. The SEM micrographs were captured on Inspect F50 (FEI Comp, the Netherlands) after sputter-coating with gold (10 nm thick). All samples consisting only ELK1 or GO were prepared for SEM imaging without a prior cross-linking process.

2.7. 3D printing of ELK1-GO materials, perfusing, and pulsating

A commercially available 3D printer (3D DISCOVERY™, RegenHU, Switzerland) was applied for the 3D printing of ELK1-GO materials. An 85 μm diameter nozzle was used to release the solution of the ELK1 (2 wt%) under 0.02–0.10 MPa pressure at a range of speed between 10 and 100 mm s^{-1}. The printing nozzle was merged in a container with 0.1% GO MilliQ water suspension. A peristaltic pulsatile pump was used to perfuse 1 v/v green food dye in MilliQ water. The perfusion speed was 12.5 ml min^{-1} and the pulse frequency was 1 Hz.

2.8. Fabrication of capillary-based permeability testing device

The device was produced by pouring a first base layer of polydimethylsiloxane (PDMS) (1 mm thickness) in a Petri dish. After curing at 60 °C for 1 h, a metal

needle of 0.8 mm outer diameter was placed on the first layer and two pins for subsequent alignment of the device. A second layer of PDMS was then poured and cured in the Petri dish. The level of PDMS in the second layer had to cover the needle. Petri dish was then placed in an oven at 60 °C for 2 h to thoroughly cure both PDMS layers. Removal of tube with forceps leaves a cylindrical cavity with a diameter of 0.8 mm. The PDMS with cavity was cut from centre and divided into two chambers. A flat membrane from an ELK1-GO tubular structure was inserted into the middle of the device and divided the channels of the left and right chambers. A test solution was injected into the right chamber, while the same solvent of the test solution was injected into the left chamber (figure S2(a)).

2.9. Permeability measurements

Two substances were used to measure permeability: fluorescein sodium salt and FITC-dextran. These two solutions were used to measure, respectively, the permeability of sodium ions and of macro molecules (20 kDa and 40 kDa). MilliQ water (phosphate-buffered saline) was injected into the left chamber and a water solution of FITC-dextran or Fluorescein sodium salt was added to the right chamber. The concentration of GO for the formation of ELK1-GO membranes was changed to observe the variations of the permeability across the membrane. The GO concentrations considered were: 0.05%, 0.10%, and 0.15%. An epi fluorescence microscope (Leica DMI 4000B, Epifluorescence Microscope with a LEICA DFC 300FXCCD camera) was used to determine the passage of molecules from one chamber of the device to another one. Data collected from the intensity analysis were described through following model:

$$C2 = \frac{V1C1}{V1+V2}\left(1 - e^{\frac{-DA(V1V2)^t}{L(V1+V2)}}\right) \quad (1)$$

where $V1$ was the volume of the left chamber, $C1$ was the concentration of molecules inside the left chamber, $V2$ was the volume of the right chamber, $C2$ was the concentration of molecules inside the right chamber; L and A were the membrane thickness and area respectively and D was the diffusion constant.

Then to determine the diffusion constant D, the experimental data were fitted with an exponential equation (equation (2)) with Matlab.

$$Y = A\left(1 - e^{-Bt}\right). \quad (2)$$

Once the diffusion constant D of the equation (equation (2)) was determined, it was compared with the argument of the exponential in model (equation (1)).

$$B = \frac{DA\,(V1V2)}{L\,(V1+V2)}. \quad (3)$$

The permeability constant (P) was calculated based on equation (4).

$$P = \frac{KD}{\Delta X} \quad (4)$$

where K is the partition constant, D is the diffusion constant, and ΔX is the thickness of the membrane.

2.10. Cell culture

GFP-Human umbilical vein endothelial cells (GFP-hUVECs) (Fisher Scientific, Angio Proteomie GFP-hUVECs, NC0601093, USA) were cultured in EGM™-2 Media (Lonza, CC-3156 and CC-4176). The medium was changed every 3 d until the cells reached 80% confluency. GFP-hUVECs between passages 2 and 4 were used for experiments. The tubes were first washed three times with PBS 8 h after assembly and sterilized with UV for 45 min. Then each tube was placed in a well of 48-well cell culture plate with inner or outer side facing up. The EGM™-2 Media (500 μl) containing different cell densities (5×10^3, 1×10^4, 5×10^4, and 1×10^5 ml^{-1}) were added to each well containing ELK1-GO membranes. The coated wells were incubated for 8 h prior to cell seeding. The cells were incubated at 37 °C and 5% CO_2 for 48 h for permeability test (figure S2(b)).

2.11. Finite elements analysis

Finite elements method simulations were carried out using COMSOL MultiPhysics® v5.5 software (license number is N. 13075339). All the presented models were developed using the Transfer of diluted species module.

2.12. Permeability model

The aim of the first model was to identify the diffusion coefficient of the membrane to dextran and sodium salt starting from experimental data. A two-dimensional (2D) axial symmetric transient model was used. Different time points were set for dextran (0 h,1 h, 3 h, 5 h) and sodium (0 min, 20 min, 40 min, 60 min) according to experimental data previously acquired. The model consists of three domains (figure S3(a)). In each domain, transport properties are governed by the following balance equations (5) and (6):

$$\frac{\partial C_i}{\partial t} + \nabla \cdot J_i = R_i \quad (5)$$

$$J_i = -D_i \nabla C_i \quad (6)$$

where C_i is the concentration (mol m^{-3}), D_i the diffusion coefficient and R_i the reaction rate. $D_i = 1 \times 10^{-9}$m^2 s^{-1} for domains 1 and 3 (same as water) while it was considered as a parameter to be estimated in the membrane (domain 2, parametric sweep study). On the right side of the membrane (domain 1) the initial concentration ($t = 0$ h min^{-1}) of salt was

1 M and 0.001 M for dextran and sodium, respectively ($C = 0$ M for other domains). A transient study allowed the evaluation of concentration profile in the whole chamber across the membrane. All external boundaries were set to no flux condition (equation (7)).

$$-n \cdot (J_i + uC_i) = 0. \tag{7}$$

For each image (acquired by epifluorescence microscope), a normalized plot profile was obtained on the centre line using ImageJ® software. The comparison between the model and the real images was carried out considering a single point in the left chamber (1 mm from the left side) (figures S3(b) and (c)). The normalized value of the grey level from the image was compared with the normalized value of the concentration in the same point of the model at different diffusion constants for each time point. Best fitting was evaluated by calculating the adjusted R-squared parameter discarding values corresponding to the membrane in both profiles (from 2 to 2.5 mm). Results are shown in figure S4.

2.13. Reaction model

The aim of this model was to identify the time of reaction between two species (aqueous solutions of 2 wt% ELK1 in 0.1 wt% GO). A 1.6 mm radius ELK1 drop in GO solution was simulated with a one-dimension (1D) axial symmetric transient model. The model consists of two domains: the first represents the ELK1 drop (initial value $C2 = 0.4$ mol m^{-3}), while the second is the GO solution ($C1 = 0.5$ mol m^{-3}) (figure S3(d)). The two species will react creating a third $C3$ species. The transport properties of the species are characterised by their diffusion constant in the different domains. We made two hypotheses:

(a) Diffusion constant of ELK1 ($C2$) and GO ($C1$) decreases linearly as $C3$ is formed according to equation (8):

$$D = D_f + D_0 \times \left(1 - {}^{c}/_{c_f}\right) \text{m}^2\ \text{s}^{-1} \tag{8}$$

where D is the diffusion at generic instant t, D_f is the final value of diffusion constant with a stable membrane, D_0 is the starting diffusion constant before the membrane formation, c is the concentration of species $C3$ at generic instant t, c_f is the concentration of the stable membrane. According to permeability model for dextran, the presence of the membrane causes a diffusivity drop of at least three orders of magnitude. We need to estimate concentration at which the membrane can be considered stable. Considering 1.5% ELK1, the protein is totally consumed forming a stable membrane, with a resulting concentration $c_f = 0.3$ mol m^{-3}. The starting diffusion coefficient (D_0) for proteins is about 10^{-9} m^2 s^{-1}, the final will be similar to that of dextran ($D_f = 1 \times 10^{-12}$m^2 s^{-1}). The final value of GO diffusion coefficient was estimated with a parametric simulation ($D_f = 1 \times 10^{-13}$, 1×10^{-15}, and 1×10^{-17}m^{2}s^{-1}; starting D_0 for GO was considered as typical values for large molecules 7×10^{-11}). On the basis of these considerations, the diffusion constant was modelled on COMSOL MultiPhysics® v5.5 with the following relation:

$$D = \max\left(D_f + D_0 \times \left(1 - {}^{c3}/_{0.3}\right), D_f\right). \tag{9}$$

Using max (x, y), if $\left(1 - {}^{c3}/_{0.3}\right) < 0$, reference diffusion constant is D_f.

(b) Diffusion of $C3$ is negligible (very low diffusion constant $D_{C_3} = 1 \times 10^{-17}$m^2 s^{-1}).

A reaction was introduced in this model in both domains. Reaction conditions were set as follows:

$$\text{d}C_1/\text{d}t = R_{c1} = -A\,(C_1 * C_2)$$

$$\text{d}C_2/\text{d}t = R_{c2} = -B\,[A\,(C_1 * C_2)]$$

$$\text{d}C_3/\text{d}t = R_{c3} = A\,(C_1 * C_2)$$

where A = reaction rate [m^3 (mol · s)$^{-1}$], B = stoichiometric ratio ELK1:GO.

The previous equations assume that:

(a) reaction rate is 200 m^3 (mol · s)$^{-1}$;
(b) since stoichiometric ratio is ELK1:GO = 20:1, $C2$ decreases 20 times faster than C1;
(c) $C3$ increases as fast as $C1$ is consumed.

On the basis of these assumptions, the reactions were modelled in COMSOL MultiPhysics® v5.5 with the following equations:

$$R_{C_1} = -200 * C_1 * C_2 * (C_1 > 0) * (C_2 > 0)$$

$$R_{C_2} = -20 * (200 * C_1 * C_2 * (C_1 > 0) * (C_2 > 0))$$

$$R_{C_3} = 200 * C_1 * C_2 * (C_1 > 0) * (C_2 > 0)$$

where the expression $[*(C_1 > 0) * (C_2 > 0)]$ means that the reaction happens only if $C1$ and $C2$ are present at the same time.

A transient study was computed over 800 s time evaluating how $C3$ is formed at the interface between $C1$ and $C2$ domains. In order to obtain a more accurate solution a user-controlled mesh was introduced by setting the maximum element size to 0.005 mm. Results are shown in figure S5.

2.14. Gradient model

The aim of this model was to identify the gradient concentration trend over time of three different GO solutions placed in a 6 cm diameter Petri dish. The three solution were 0.05%, 0.10%, and 0.15% GO w/v respectively, corresponding to 0.25, 0.5 and 0.75 mol m^{-3} (MW of GO is 2043.8 g mol^{-1}). A 2D transient model consisting of four domains was developed: domain 1 corresponds to water, while 2, 3 and 4 are the three different GO solutions placed with increasing concentration value (figure S3(e)). Diffusion constant was set to $D_i = 1 \times 10^{-9} m^2 s^{-1}$ (same as water). Concentration trend over a 96 h time was evaluated on a cut line placed in the middle of the Petri dish (red line in figure S3(e)).

3. Results and discussion

3.1. Rationale of the study

Our previous research demonstrated that, upon printing a solution of ELK1 into another of GO (figure 1(a)), hydrophobic and electrostatic interactions trigger ELK1-GO co-assembly and an interfacial diffusion-reaction process that gives rise to a multilayered membrane (figure 1(b)). In the current work, we study in more detail the diffusion-reaction process to better control the ELK1-GO co-assembly, formation of the tubular structure, and the properties of the interfacial membrane including thickness, porosity, and permeability. By modulating the way in which both solutions are mixed, it is possible to spatially control this process and generate hierarchical tubular structures by integrating bottom-up assembly with top-down manufacturing. Furthermore, by standardizing together both the printing and co-assembling parameters, the system enables control over the printability, shape fidelity, and ultimate feature resolution (i.e. tube diameter and tube wall thickness) of the bioink. Through this approach, the resulting material (i.e. tube wall) can be designed to exhibit a variety of physiologically-relevant properties such as tuneable thickness (down to ~2 μm), stiffness, permeability, and the ability to be robust and compliant, evidenced by the capacity to pulsate under physiological fluid flow (i.e. shear stress of ~0.26 N m^{-2}, which is within the range of that present in carotid arteries [30]) (figure 1(f) and movie S1) and be bent without displaying any kinks (figure 1(g) and movie S2). Consequently, we first conducted experiments and simulations to characterize, standardize, and optimize the printing parameters. We then focused on further controlling the printing fidelity and material properties by modulating the concentration of GO. Given the potential use of the bioink to fabricate perfusable fluidic systems and structures that can recreate biological ones, we then conducted a thorough characterization of tube wall permeability with and without cells as well as developed ways to fabricate structures with tuneable and anisotropic permeability.

3.2. Standardization and optimization of the printing process

Standardization and optimization experiments were conducted by integrating top-down (3D printing) and bottom-up (self-assembly) fabrication parameters to maximize printing fidelity and control over resulting geometric features.

3.2.1. ELK1-GO diffusion-reaction process and printing fidelity

We conducted experiments and simulations to characterize bioink shape fidelity as determined by the diffusion-reaction mechanism triggered upon ELK1-in-GO printing. First, an 18 μl aqueous solution of ELK1 (2 wt%) was manually injected into an aqueous suspension of GO (0.10 wt%, 100 μl) in a 96-well plate to generate a vertical tube. The process was video recorded (figure S1) and imaged at different timepoints to investigate the kinetics of tube wall formation (figure 2(a)) and movie S2). Separately, a 'transport of diluted species' COMSOL model simulating similar experimental conditions was generated and used to validate the experimental results. Both experimental and simulation results were in agreement and revealed that the ELK1-GO tube exhibited a similar diameter as that of the starting ELK1 injected drop and the ELK1-GO tube wall thickness did not increase after ~60 s of interaction (figure 2(a), figure S5). These results demonstrate that the initial volume of the ELK1 injection determined the outside dimension of the final printed structure (figure 2(a)) and that this dimension was not affected by the growth of the ELK1-GO interfacial tube wall as a result of its diffusion-reaction process.

3.2.2. Tuneable geometry by varying printing parameters and GO concentration

The printability of the ELK1-GO bioink was characterized using a commercially available 3D printer (3D Discovery™, RegenHU, Switzerland) with adjustable nozzle heights and diameters, dispensing pressures, and printing speeds [31]. By fixing nozzle height and diameter, we assessed the relation between dispensing pressure and printing speed. The fidelity of fabricated ELK1-GO tubes was assessed by optically and systematically measuring tube diameters at different locations [32], which revealed increased printing fidelity with increasing printing speed (figures 2(b) and (c)). Larger diameter differences within a single tube led to larger variances, which resulted in rugged tube walls (figure 2(b), printing speed: 10 mm s^{-1}). By varying the dispensing pressure of the ELK1 solution between 0.02 and 0.10 MPa and the printing speed (PS) between 10 and 100 mm s^{-1} (nozzle height and diameter were fixed, figure 2(b), table), we found that tubes were generated when the dispensing pressure was between 0.04 and 0.08 MPa. When printing within this pressure range and printing speeds above 30 mm s^{-1}, variances in tube wall geometry within a

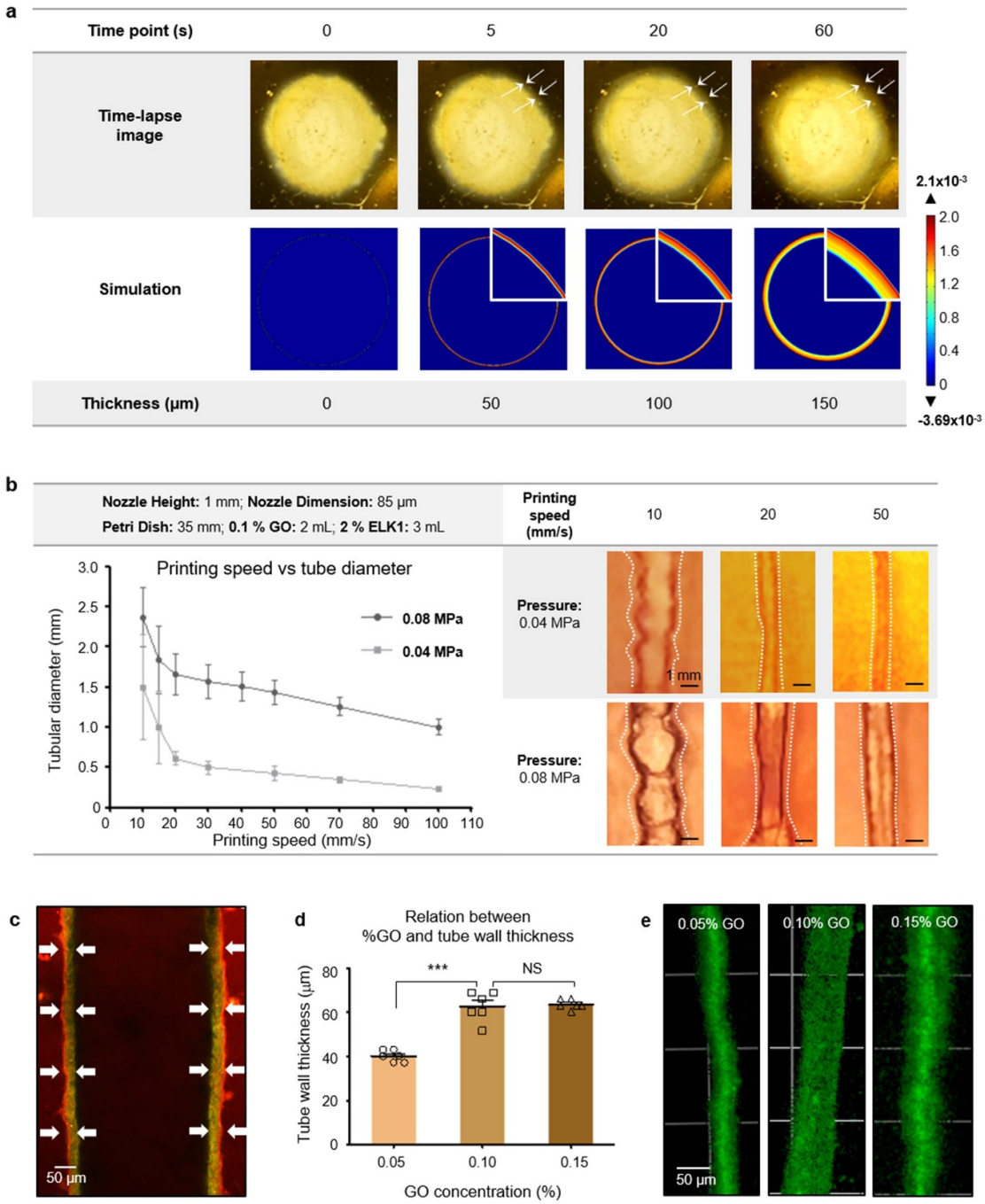

Figure 2. Diffusion-reaction process and printing fidelity. (a) Time-lapse optical images of a co-assembling tube upon immersion of a solution of ELK1 into a solution of GO depicting a growing tube wall (shown between white arrows) reaching a maximum of ∼150 μm in thickness after ∼60 s. In the bottom row, corresponding images of tube wall thickness from 'transport of diluted species' COMSOL model simulations (rainbow colour) confirming the increasing thickness of the tube wall as a result of the time-dependent diffusion-reaction process of formation. (b) The graph on the left reports on the relationship between printing speed, releasing pressure, and fabricated tube diameters. Error bars represent ±SD for $n = 10$. $^*p < 0.05$. t test. The images on the right illustrate the printing fidelity of the ELK1-GO bioink in relation to different printing parameters. (c) Confocal image of a longitudinal-section of an ELK1-GO depicting the tube walls (between white arrows) (green = ELK1, red = GO) demonstrating a high-fidelity tubular structure. (d). Graphs and €. Corresponding confocal images of unilateral longitudinal-sections of the wall of ELK1-GO tubes revealing the relationship between the concentration of the GO suspension prior to co-assembly and the resulting tube wall thickness. ±SD for $n = 5$. $^*p < 0.05$. t test.

single tube were under 5%, which reflected high fidelity tubes with smooth walls (figure 2(b)). Utilizing a dispensing pressure of 0.06 MPa and printing speed of 30 mm s^{-1}, we were able to print tubes of up to 12 cm in length and 2 mm in diameter. It is important to mention, however, that the limitation on tube length was not lack of tube integrity but rather the size of the plate used to hold the GO solution during printing.

Printing fidelity was also characterized by varying the concentration of the GO suspension (figure 2(c)). In this case, lower concentrations of GO (0.05 wt%)

generated tubes with lower printing fidelity and thinner tube walls (~40 μm), while higher GO concentrations (0.10 and 0.15 wt%) resulted in tubes with higher printing fidelity and thicker walls (~60 μm) (figures 2(d) and (e)). We speculate that this difference in wall thickness results from interfacial membranes forming with varying levels of permeability as a result of having different concentrations of GO. We have demonstrated that upon initial ELK1-GO co-assembly, a diffusion barrier is formed, which defines its downstream diffusion-reaction mechanism that generates the distinctive multilayer membrane [29]. We reason that lower concentration of GO (0.05 wt%) leads to a more permeable diffusion barrier, which allows for higher and faster ELK1 diffusion and consequently thinner multi-layered membranes. In contrast, higher concentration of GO (0.15 wt%) upon co-assembly results in the formation of a less permeable diffusion barrier, which results in thicker membranes.

3.2.3. Tuneable porosity by varying the concentration of GO suspension

Having characterized printing reproducibility and fidelity, we then focused on exploiting the co-assembling nature of the bioink to control ELK1-GO tube wall porosity by varying the concentration of GO. Tubes were first co-assembled with varying GO concentrations (0.05 wt%, 0.10 wt%, and 0.15 wt%) and cut to extract flat membranes (the tube wall) (figure S1(a)). The luminal (inner) and abluminal (outer) sides of these membranes were then examined by SEM following standard preparation protocols [29]. As expected, increased GO concentrations led to decreased porosity, which was easily noticeable on both inner and outer surfaces of the membranes (figure 3(a)). Upon closer inspection, significant differences in porosity between the inner and outer surfaces were observed on all membranes, independently of GO concentration (figure 3(b)), which was also confirmed by histological sectioning (figure 3(d)). These results demonstrated the possibility to modulate the ELK1-GO tube wall pore sizes from 0.5 to 1.2 μm on the inner surface and 1.6–4.0 μm on the outer one by modifying GO concentrations (figure 3(c)).

Together with the previous results of printing fidelity and tuneability of geometry and porosity, we can conclude that higher GO concentration and printing speed (50 mm s^{-1} < PS < 70 mm s^{-1}) can be used to fabricate higher fidelity tubes with smooth and thicker (~60 μm) fully formed tube walls but less porosity after 60 s of co-assembly. By contrast, lower GO concentration and printing speed (30 mm s^{-1} < PS < 50 mm s^{-1}) would generate lower fidelity tubes with rugged and thinner (~40 μm) tube walls exhibiting higher levels of porosity. Importantly, upon ELK1-GO co-assembly, the thickness of the resulting interfacial structures depends on the time-dependent diffusion-reaction process of formation (figure 2(a)). Consequently, given the high ELK1-GO affinity, it is possible to stop the co-assembly process at different time points, resulting in interfacial membranes of different thicknesses. We found that it was possible to stop the co-assembly process after just 15 s by removing the fabricated tube from the GO suspension, resulting in tube wall thicknesses down to ~2 μm when printing at >70 mm s^{-1}. Furthermore, tube wall thicknesses were observed to reach a maximum of ~20 μm in thickness (figure 2(c)) after ~60 s of co-assembly, which did not seem to change after longer periods of time. We speculate that these thin tube walls result from the low ELK1 volumes released upon printing at fast printing speeds (>70 mm s^{-1}), offering an opportunity to reproducibly fabricate with resolutions down to a few microns in size (figures 1(c) and (d)). In summary, these results demonstrate how bioprinting fidelity and resolution can be tuned through both printing parameters from the top-down and self-assembling events taking place from the bottom-up.

3.3. Assessment of applicability

After standardization of fabrication parameters, we then focused on demonstrating applicability and key advantages of the bioink including the capacity to tailor permeability, display pulsatility, and fabricate structures exhibiting anisotropic permeability.

3.3.1. Tuneable permeability by varying porosity

The possibility to control tube wall porosity opens an opportunity to fabricate membranes, capillaries, and other structures with tuneable permeability that could be designed to recreate that of biological tissues. For example, proper vascular permeability is of outmost importance in many biological processes such as regulating diffusion of nutrients and waste products, serving as a semipermeable barrier between blood contents and tissues to screen toxic molecules, and regulating the microenvironment of the ECM [33]. Furthermore, diffusion across vascular and lymphatic tissues is vital to enable appropriate filtration, protection, and delivery of key solutes, cells, and factors. The capacity to develop vascular structures or fluidic devices with tuneable permeability is critical to recreate and optimize biofunctionality. To assess the effect of tube wall porosity on its permeability, we designed a simple capillary-based permeability testing device where the membrane (cut from the ELK1-GO tube) can be positioned in the middle, leaving two free chambers on either side (figure S2(a)). The chambers can be filled with any solution, enabling diffusion of solutes from one side to the other (figure S2(a)). We tested the permeability of the membrane to fluorescein sodium salt and 20 kDa FITC-dextran in water solution to recreate physiological charge and size

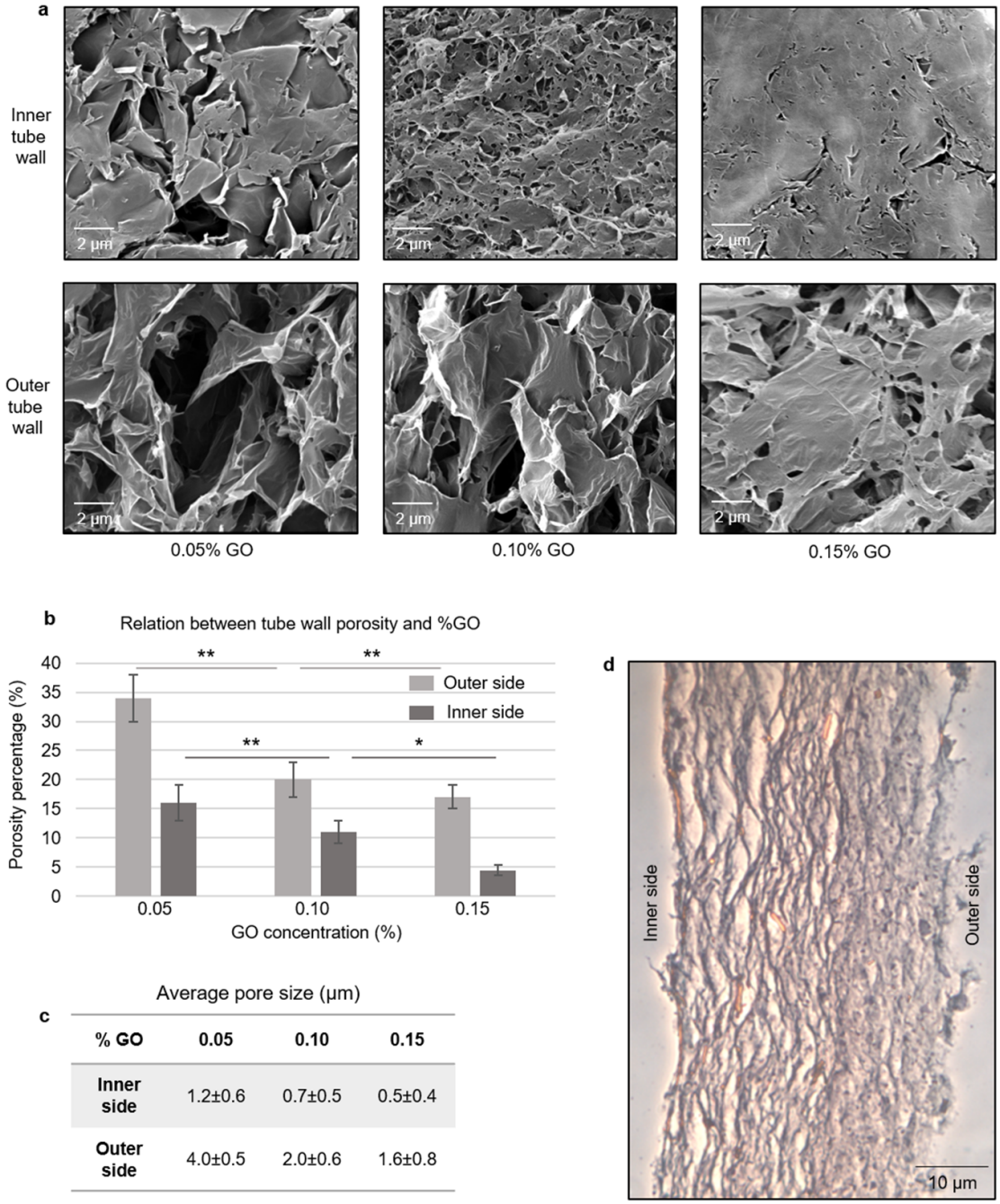

Figure 3. Control of tube wall porosity by varying the concentration of GO. (a). SEM images and b, c corresponding quantifications of porosity (b) and pore size, (c) demonstrating significant differences in porosity between the inner and outer surfaces on all membranes (tube walls) and pore sizes by modifying GO concentration. (d) Histological slide of tube wall cross-section demonstrating the decrease in porosity from the inner side of the tube wall to the outer side of the tube wall. ±SD for $n = 3$. $^{*}p < 0.05$. t test.

barriers, respectively. These two functions are normally observed in vascular tissue [33]. Using epifluorescence microscopy imaging, permeability constants were calculated based on the fluorescence intensity profiles recorded on the chamber where the solutes diffused to (figure 4(a)). Specifically, exponential curves describing the trend of the average intensity within the chamber as a function of time were calculated for each ELK1-GO membrane and the permeability constant measured based on a diffusion constant using a fitting plot [34] (figure 4(b)).

To confirm these results, we established a 'transport of diluted species' COMSOL model to predict the permeability of sodium salt through the membrane (figure 4(a)). Similar to the experimental setup, sodium salt exhibited faster diffusion than 20 kDa FITC-dextran (figure 4(c)) with a permeability constant of $\sim 5 \times 10^{-5}$ cm s^{-1}. Furthermore, as expected, we found that the permeability constants decreased with increasing concentration of GO for both fluorescein sodium salt (from 1×10^{-5} cm s^{-1} to 5×10^{-5} cm s^{-1}) and 20 kDa FITC-dextran

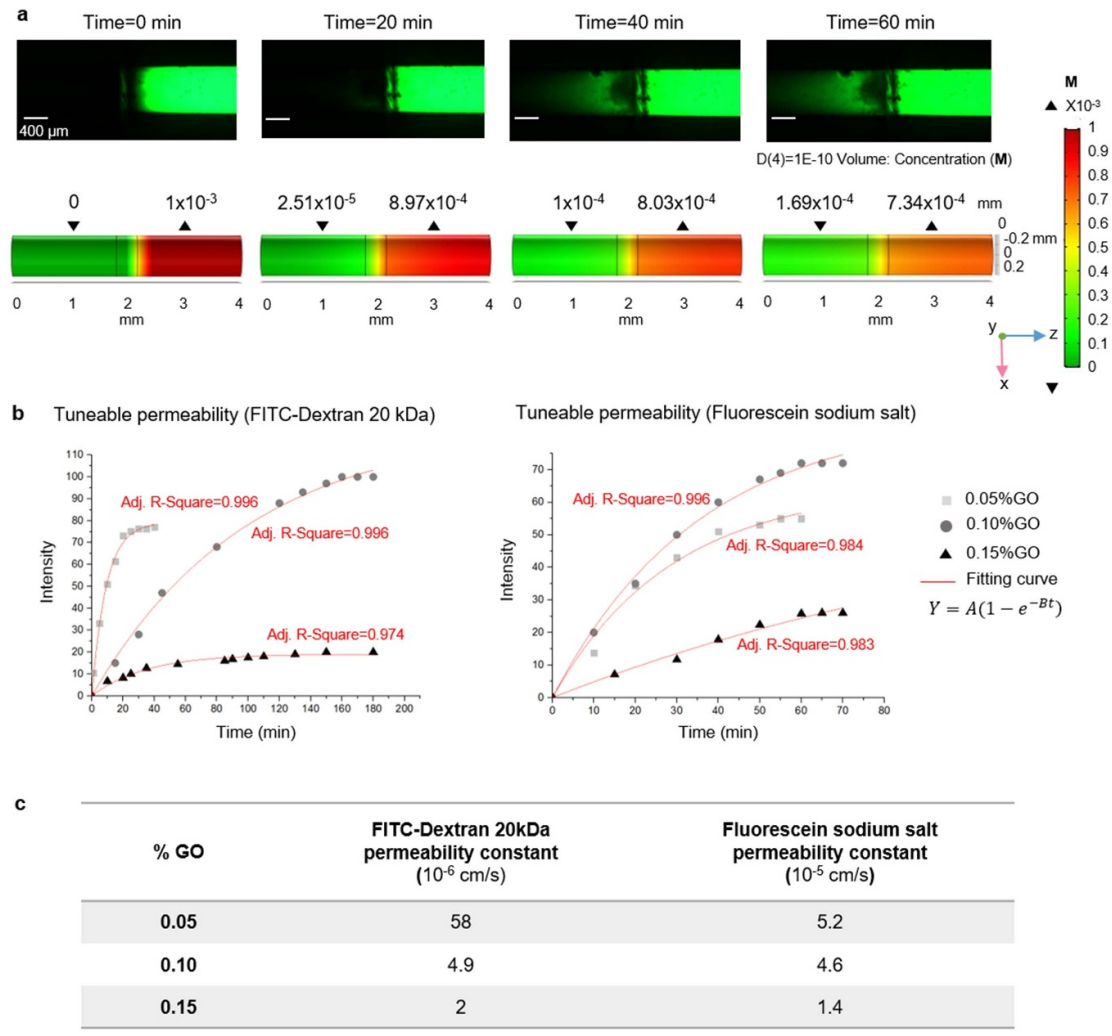

c

% GO	FITC-Dextran 20kDa permeability constant (10^{-6} cm/s)	Fluorescein sodium salt permeability constant (10^{-5} cm/s)
0.05	58	5.2
0.10	4.9	4.6
0.15	2	1.4

Figure 4. Control of tube wall permeability by varying the concentration of GO. (a) Confocal images and corresponding 'transport of diluted species' COMSOL model simulations of a perfused ELK1-GO membrane (cut from an ELK1-GO tube) positioned in the middle of a capillary-based permeability testing device. Upon injection of fluorescein sodium salt solution in the right chamber, progressive diffusion across the membrane is observed at different time points in the left chamber. In the bottom, red colour indicating high fluorescein sodium salt concentration while green colour indicating low concentration. (b) Graphs depicting the time-dependent fluorescein density change of FITC-dextran 20 kDa (left) and fluorescein sodium salt (right) in the left chamber of the permeability testing device with fitting lines. (c) Permeability constants calculated based on the data reported in (b) revealing the permeabilities of ELK1-GO membranes for FITC-dextran 20 kDa and fluorescein sodium salt decrease with the increasing concentration of GO suspension.

(from 2×10^{-6} cm s^{-1} to 58×10^{-6} cm s^{-1}) (figure 4(c)).

These results demonstrate the potential of the ELK1-GO bioink to fabricate membranous and tubular structures while enabling regulation of permeability. By simply modulating GO concentration, it is possible to fabricate complex structures made from thin membranes with permeability constants comparable to those of the native retina ($\sim 2 \times 10^{-5}$ cm s^{-1}) [35], lymphatic-vessels ($\sim 6.4 \times 10^{-6}$cm s^{-1}) [36], an hUVEC-containing Transwell ($\sim 5 \times 10^{-6}$ cm s^{-1}) [37], and organ-on-chip devices of the blood-brain-barrier ($\sim 5 \times 10^{-5}$ cm s^{-1}) [38].

3.3.2. Tuneable permeability after endothelialisation

In our previous study, we demonstrated how the ELK1-GO self-assembling system can be incorporated within liquid-in-liquid printing to biofabricate tubular structures comprising cells exhibiting high viability and growth for at least 7 d [29]. To demonstrate the functionality and biological relevance of the bioink, we conducted similar permeability tests but after endothelialisation of the lumen of the ELK1-GO tubes. This setup enabled us to better account for the localization of the cells and their effect on tube-wall permeability. Different densities (5×10^3, 1×10^4, 5×10^4, or 1×10^5 ml^{-1}) of hUVECs were seeded on the luminal side of membranes (cut from ELK1-GO tubes) (0.10 wt% GO) placed on Petri dishes (figure S2(b), top). We chose the method of seeding hUVECs after tube formation instead of directly co-assembling with cells to more precisely account for the localization of the cells, their interaction, and the resulting effect on permeability. As expected, after 48 h of culture,

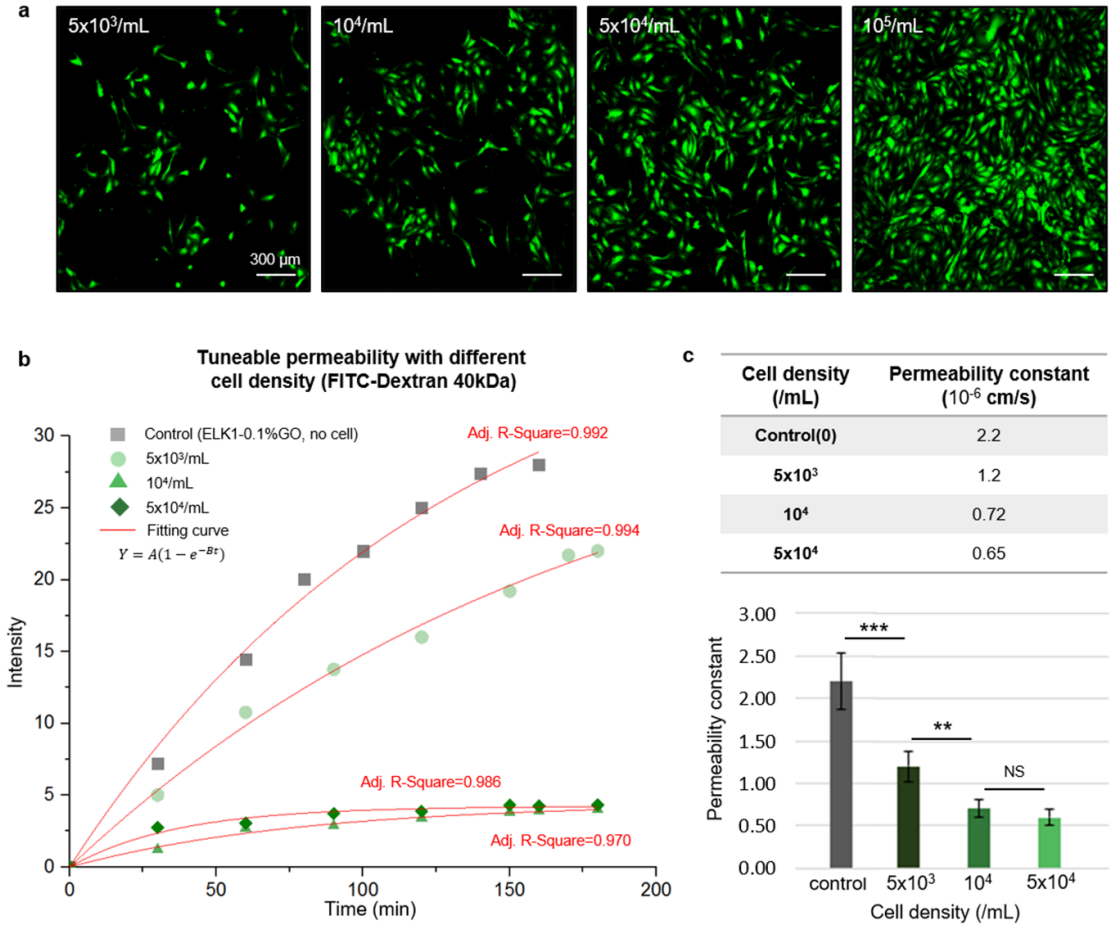

Figure 5. Modification of permeability after endothelialisation. (a) Confocal images of hUVECs (green) grown at different confluency levels (left to right: 30%, 50%, 80%, >95%) on the inner side of ELK1-GO membranes. (b) Graphs recording the fluorescein density change of FITC-dextran 40 kDa with time in the left chamber with fitting lines and (c). Permeability constants calculated based on the data reported in (b) for FITC-dextran 40 kDa permeability through ELK1-GO-hUVECs membranes. Membrane permeability tended to decrease with increased cell density, with membranes without cells (control) exhibiting the highest permeability constant while those with the highest cell density exhibiting the lowest one. ±SD *for* $n = 3$. $^*p < 0.05$. *t* test.

membranes exhibited different hUVEC densities including ∼30%, 50%, 80%, and >95%, as measured by confocal microscopy imaging (figure 5(a), confocal images). Then, these membranes were inserted into the permeability test device with hUVECs facing one of the chambers (figure S2(b), bottom). Then, 40 kDa FITC-dextran [39] in phosphate-buffered saline (PBS) was flowed into the chamber facing the cells while PBS alone was flowed into the other. Here, we used 40 kDa FITC-dextran instead of the 20 kDa FITC-dextran as it is widely used to test biomaterial permeability [39]. The results demonstrated that membrane permeability tended to decrease with increased cell density, with membranes without cells (control) exhibiting the highest permeability constant (2.2×10^{-6} cm s^{-1}) while those with the highest cell density exhibited the lowest permeability constant (6.5×10^{-7} cm s^{-1}) (figures 5(b) and (c)). In conclusion, the presence of hUVECs growing on the ELK1-GO tube wall significantly influenced the transport of solutes in a way that is dependent on the level of hUVEC confluency. We speculate that lower cell densities led to lower number of endothelial cell junctions, which in turn led to higher permeabilities. These results further support the possibility to tune structure permeability and, in particular, to do it through the presence of cells. For example, the permeability constant of ELK1-GO-hUVEC membranes ($\sim 1 \times 10^{-6}$ cm s^{-1}) with confluence levels above 50% were comparable with that of tumour micro vessels (1.8×10^{-6} cm s^{-1}) [40].

The possibility to rapidly and controllably engineer living capillary- and vascular-like structures remains a major unmet challenge in biofabrication, tissue engineering, and *in vitro* models. Feng *et al* have demonstrated how liquid-in-liquid printing can be used to fabricate perfusable tubular structures [24] but the system relies on aqueous nanoclay dispersions and solutions of H2N-PDMS-NH2 in toluene, which prevents the use of cells and recreation of key anatomical and physiological features. On the other hand, perfusable channels within bulk gel structures have been reported by Skylar-Scott *et al* [41], but these structures fail to recapitulate capillary features such as an outside surface and thin wall thicknesses, which consequently affect biomechanics

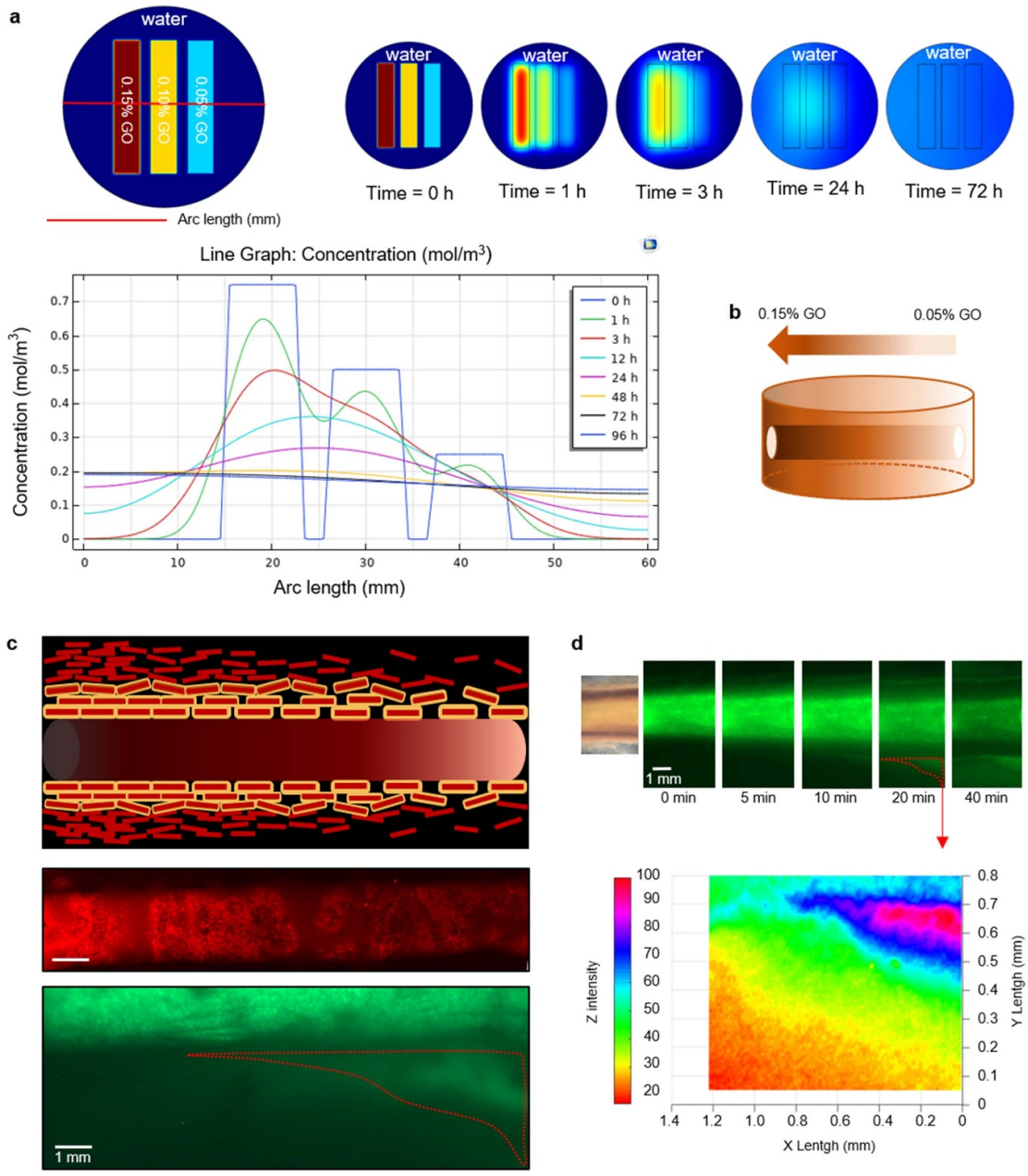

Figure 6. Fabrication of tubular structures with anisotropic porosity and permeability. (a) Images of 'transport of diluted species' COMSOL model simulations and corresponding graphs demonstrating the maintained gradient of increasing GO concentration in solution for at least 3 h. (b) Illustration of the mechanism of fabricating the tubular structures with progressively decreasing porosity and permeability by printing the ELK1 solution from right to left into the GO solutions. (c) Schematic of the fabrication process and mechanism of assembly of a tubular structure with progressively increasing concentration of GO. GO was stained with Rhodamin B (red, middle image) prior to printing of the ELK1 solution to enable GO visualization within the tube wall. After ELK1-GO tube fabrication, FITC-dextran 20 kDa (green, bottom image) was perfused through the tube and was observed to diffuse in time through the tube wall with higher levels of diffusion in the areas of the tube with lower concentration of GO (qualitatively increasing diffusion from left to right). (d) Optical microscope image and time-lapse confocal images of the perfused tube with FITC-dextran 20 kDa (green) at different times points. A fluorescent intensity analysis on the permeated area outside the tube (*X* axis = parallel to the tube axis, *Y* axis = perpendicular to the tube axis) confirming the anisotropic permeability variance at different time points.

and diffusion kinetics. Our system aims to overcome some of these challenges by providing a facile way to manufacture biohybrid capillary-like structures with physiological properties.

3.3.3. Fabrication of tubular structure with anisotropic porosity and permeability

To further demonstrate the potential of the self-assembling ELK1-GO bioink for the biofabrication of complex structures with innovative properties, we printed tubes but now exhibiting different porosities and corresponding permeabilities within the same structure along the tube axis (figure 6(c), illustrator). These types of structures are observed in biological systems such as renal tubules [42] and arteriovenous networks [43]. To our knowledge, these structures have not been fabricated in a single printing process. We first designed an experimental setup that enabled

the formation of a MilliQ water solution made with different concentrations of GO contiguously increasing from 0.15 wt% on the left side, 0.10 wt% on the middle, and 0.05 wt% on the right side (figure 6(a)). The GO was stained with Rhodamin B prior to printing of the ELK1 to enable GO visualization in the tube wall. In this setup, we found that the gradient of the GO in solution was maintained for at least 3 h, which was confirmed by a 'transport of diluted species' COMSOL model (figure 6(a)) and facilitated the printing process. Upon extrusion of the ELK1 solution into the GO solution from the lower to the higher concentration of GO, the tube formed immediately at the interface of both liquids with the tube wall progressively assembling with increasing concentrations of GO (figure 6(b)). The resulting tubular structure was then characterized via epifluorescence microscopy, which revealed a tube wall with increasing content of GO and consequently a porosity gradient (figure 6(c), red). To test the effect of this porosity gradient on the permeability of the overall tube, 20 kDa FITC-dextran solution was perfused through and, as expected, its diffusion progressively decrease along the tube direction as the GO concentration increased (figures 6(c), green and (d)). These kinds of anisotropic structures are prevalent in biological systems such as in renal tubules [42] and arteriovenous networks [43]. Our bioink enables the fabrication of such anisotropic vascular structures in a simple manner.

4. Conclusion

Self-assembling bioinks offer unique opportunities to the field of biofabrication. However, it is essential to establish reproducible processes, optimize printing parameters, and demonstrate their ability to fabricate novel structures with anatomical and physiological relevance. Here, we have standardized and optimized a multicomponent self-assembling bioink and demonstrated its potential to biofabricate structures with innovative properties. Through experimental work and simulations, we have confirmed the possibility to use the ELK1-GO bioink to fabricate a single tubular structure with hierarchical organization and resolutions down to $\sim$10 μm in diameter made with $\sim$2 μm thick walls. These structures enable immediate perfusion after assembly and exhibit physical properties such as stiffnesses and the capacity to pulsate that resemble physiological structures. In addition, the bioink permits printing fidelity and control over structure porosity and permeability by modulating the concentration of GO and the possibility to guide this process to fabricate structures with permeability gradients. Furthermore, the bioink is biocompatible and facilitates hUVEC bioprinting, growth, and proper function, enabling further control of permeability. However, to fully exploit these advantages, it is of outmost importance to incorporate the printing/self-assembling processing and structures reported here within functional devices such as tissue engineered constructs or organ-on-chip devices. Nonetheless, the current work moves us a step closer towards the scalable manufacturing of structurally complex capillary-based constructs that can be designed to recreate the structural and permeability properties of native tissues within engineered devices.

Acknowledgments

The work was supported by the ERC Starting Grant (STROFUNSCAFF), the Medical Research Council (UK Regenerative Medicine Platform Acellular/Smart Materials 3D Architecture, MR/R015651/1), and the AO Foundation AOCMF-17-19M. We thank Dr J Rafael Castrejón-Pita from the School of Engineering and Materials Science at Queen Mary University of London for offering devices to record optical images of diffusion reaction. We thank Mr Jingyu Feng from Department of Chemical Engineering at Imperial College London for helping design illustrator of capillary-based permeability testing device.

ORCID iDs

Yuanhao Wu https://orcid.org/0000-0002-3955-6474
Gabriele Maria Fortunato https://orcid.org/0000-0002-0260-4014
Babatunde O Okesola https://orcid.org/0000-0003-0392-9205
John Connelly https://orcid.org/0000-0002-5955-8848
Carmelo De Maria https://orcid.org/0000-0002-1368-3571
Jose Carlos Rodriguez-Cabello https://orcid.org/0000-0002-3438-858x
Giovanni Vozzi https://orcid.org/0000-0002-9414-9994
Wen Wang https://orcid.org/0000-0002-6913-4731
Alvaro Mata https://orcid.org/0000-0002-6739-9111

References

[1] Schwab A, Levato R, D'Este M, Piluso S, Eglin D and Malda J 2020 Printability and shape fidelity of bioinks in 3D bioprinting *Chem. Rev.* **120** 11028–55
[2] Kolesky D B, Homan K A, Skylar-Scott M A and Lewis J A 2016 Three-dimensional bioprinting of thick vascularized tissues *Proc. Natl Acad. Sci. USA* **113** 3179–84
[3] Kim S H *et al* 2018 Precisely printable and biocompatible silk fibroin bioink for digital light processing 3D printing *Nat. Commun.* **9** 1620
[4] Ashammakhi N, Ahadian S, Xu C, Montazerian H, Ko H, Nasiri R, Barros N and Khademhosseini A 2019 Bioinks and

bioprinting technologies to make heterogeneous and biomimetic tissue constructs *Mater. Today Biol.* **1** 100008
[5] Da Silva K, Kumar P, Choonara Y E, Du Toit L C and Pillay V 2020 Three-dimensional printing of extracellular matrix (ECM)-mimicking scaffolds: a critical review of the current ECM materials *J. Biomed. Mater. Res.* A **108** 2324–50
[6] Won J E, Lee Y S, Park J H, Lee J H, Shin Y S, Kim C H, Knowles J C and Kim H W 2020 Hierarchical microchanneled scaffolds modulate multiple tissue-regenerative processes of immune-responses, angiogenesis, and stem cell homing *Biomaterials* **227** 119548
[7] Rose J C and De Laporte L 2018 Hierarchical design of tissue regenerative constructs *Adv. Healthcare Mater.* **7** 1701067
[8] Morgan F L C, Moroni L and Baker M B 2020 Dynamic bioinks to advance bioprinting *Adv. Healthcare Mater.* **9** 1901798
[9] Gungor-Ozkerim P S, Inci I, Zhang Y S, Khademhosseini A and Dokmeci M R 2018 Bioinks for 3D bioprinting: an overview *Biomater. Sci.* **6** 915–46
[10] Mendes A C, Baran E T, Reis R L and Azevedo H S 2013 Self-assembly in nature: using the principles of nature to create complex nanobiomaterials *Wiley Interdiscip. Rev. Nanomed. Nanobiotechnol.* **5** 582–612
[11] Okesola B O and Mata A 2018 Multicomponent self-assembly as a tool to harness new properties from peptides and proteins in material design *Chem. Soc. Rev.* **47** 3721–36
[12] Raymond D M and Nilsson B L 2018 Multicomponent peptide assemblies *Chem. Soc. Rev.* **47** 3659–720
[13] Hedegaard C L, Redondo-Gómez C, Tan B Y, Ng K W, Loessner D and Mata A 2020 Peptide-protein coassembling matrices as a biomimetic 3d model of ovarian cancer *Sci. Adv.* **6** eabb3298
[14] Brennan J R and Hocking D C 2016 Cooperative effects of fibronectin matrix assembly and initial cell-substrate adhesion strength in cellular self-assembly *Acta Biomater.* **32** 198–209
[15] Derkus B, Okesola B O, Barrett D W, D'Este M, Chowdhury T T, Eglin D and Mata A 2020 Multicomponent hydrogels for the formation of vascularized bone-like constructs *in vitro Acta Biomater.* **109** 82–94
[16] Hellmund K S and Koksch B 2019 Self-assembling peptides as extracellular matrix mimics to influence stem cell's fate *Front. Chem.* **7** 172
[17] Arab W, Rauf S, Al-Harbi O and Hauser C A E 2018 Novel ultrashort self-assembling peptide bioinks for 3D culture of muscle myoblast cells *Int. J. Bioprinting* **4** 129
[18] Choudhury D, Tun H W, Wang T and Naing M W 2018 Organ-derived decellularized extracellular matrix: a game changer for bioink manufacturing? *Trends Biotechnol.* **36** 787–805
[19] Hedegaard C L, Collin E C, Redondo-Gómez C, Nguyen L T H, Ng K W, Castrejón-Pita A A, Castrejón-Pita J R and Mata A 2018 Hydrodynamically guided hierarchical self-assembly of peptide-protein bioinks *Adv. Funct. Mater.* **28** 1703716
[20] Raphael B, Khalil T, Workman V L, Smith A, Brown C P, Streuli C, Saiani A and Domingos M 2017 3D cell bioprinting of self-assembling peptide-based hydrogels *Mater. Lett.* **190** 103–6
[21] Loo Y, Lakshmanan A, Ni M, Toh L L, Wang S and Hauser C A E 2015 Peptide bioink: self-assembling nanofibrous scaffolds for three-dimensional organotypic cultures *Nano Lett.* **15** 6919–25
[22] Lee M, Bae K, Levinson C and Zenobi-Wong M 2020 Nanocomposite bioink exploits dynamic covalent bonds between nanoparticles and polysaccharides for precision bioprinting *Biofabrication* **12** 25025
[23] Hedegaard C L and Mata A 2020 Integrating self-assembly and biofabrication for the development of structures with enhanced complexity and hierarchical control *Biofabrication* **12** 032002
[24] Feng W, Chai Y, Forth J, Ashby P D, Russell T P and Helms B A 2019 Harnessing liquid-in-liquid printing and micropatterned substrates to fabricate 3-dimensional all-liquid fluidic devices *Nat. Commun.* **10** 1095
[25] Luo G, Yu Y, Yuan Y, Chen X, Liu Z and Kong T 2019 Freeform, reconfigurable embedded printing of all-aqueous 3D architectures *Adv. Mater.* **31** 1904631
[26] Forth J, Liu X, Hasnain J, Toor A, Miszta K, Shi S, Geissler P L, Emrick T, Helms B A and Russell T P 2018 Reconfigurable printed liquids *Adv. Mater.* **30** 1707603
[27] Chen A H and Silver P A 2012 Designing biological compartmentalization *Trends Cell Biol.* **22** 662–70
[28] Inostroza-Brito K E *et al* 2015 Co-assembly, spatiotemporal control and morphogenesis of a hybrid protein-peptide system *Nat. Chem.* **7** 897–904
[29] Wu Y *et al* 2020 Disordered protein-graphene oxide co-assembly and supramolecular biofabrication of functional fluidic devices *Nat. Commun.* **11** 1182
[30] Hoeks A P G, Samijo S K, Brands P J and Reneman R S 1995 Noninvasive determination of shear-rate distribution across the arterial lumen *Hypertension* **26** 26–33
[31] Yin J, Zhao D and Liu J 2019 Trends on physical understanding of bioink printability *Bio-Design Manuf.* **2** 50–54
[32] Lee J M and Yeong W Y 2020 Engineering macroscale cell alignment through coordinated toolpath design using support-assisted 3D bioprinting *J. R. Soc. Interface* **17** 20200294
[33] Ono S, Egawa G and Kabashima K 2017 Regulation of blood vascular permeability in the skin *Inflamm. Regen.* **37** 11
[34] Montemurro F, De Maria C, Orsi G, Ghezzi L, Tinè M R and Vozzi G 2017 Genipin diffusion and reaction into a gelatin matrix for tissue engineering applications *J. Biomed. Mater. Res.* B **105** 473–80
[35] Tsuboi S, Fujimoto T, Uchihori Y, Emi K, Iizuka S, Kishida K and Manabe R 1984 Measurement of retinal permeability to sodium fluorescein *in vitro Investigative Ophthalmol. Vis. Sci.* **25** 1146–50
[36] Sato M, Sasaki N, Ato M, Hirakawa S, Sato K and Sato K 2015 Microcirculation-on-a-chip: a microfluidic platform for assaying blood-and lymphatic-vessel permeability *PLoS One* **10** e0137301
[37] Glod J, Kobiler D, Noel M, Koneru R, Lehrer S, Medina D, Maric D and Fine H A 2006 Monocytes form a vascular barrier and participate in vessel repair after brain injury *Blood* **107** 940–6
[38] Gaillard P J and De Boer A G 2000 Relationship between permeability status of the blood-brain barrier and *in vitro* permeability coefficient of a drug *Eur. J. Pharm. Sci.* **12** 95–102
[39] Kirschner N, Rosenthal R, Furuse M, Moll I, Fromm M and Brandner J M 2013 Contribution of tight junction proteins to ion, macromolecule, and water barrier in keratinocytes *J. Investigative Dermatol.* **133** 1161–9
[40] Reitan N K, Thuen M, Goa P E and De Lange Davies C 2010 Characterization of tumor microvascular structure and permeability: comparison between magnetic resonance imaging and intravital confocal imaging *J. Biomed. Opt.* **15** 036004
[41] Skylar-Scott M A, Uzel S G M, Nam L L, Ahrens J H, Truby R L, Damaraju S and Lewis J A 2019 Biomanufacturing of organ-specific tissues with high cellular density and embedded vascular channels *Sci. Adv.* **5** eaaw2459
[42] Verkman A S 1989 Mechanisms and regulation of water permeability in renal epithelia *Am. J. Physiol. Cell Physiol.* **257** C837
[43] Fish J E and Wythe J D 2015 The molecular regulation of arteriovenous specification and maintenance *Dev. Dyn.* **244** 391–409